

# Nanoscale Engineering of Closely-Spaced Electronic Spins in Diamond

Diego Scarabelli,<sup>†</sup> Matt Trusheim,<sup>‡</sup> Ophir Gaathon,<sup>§</sup> Dirk Englund,<sup>\*,‡</sup> and Shalom J. Wind<sup>\*,†</sup>

<sup>†</sup>Department of Applied Physics and Applied Mathematics, Columbia University, New York, New York 10027, United States

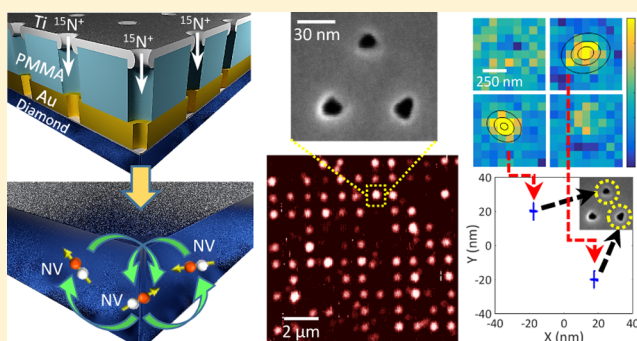
<sup>‡</sup>Department of Electrical Engineering and Computer Science, Massachusetts Institute of Technology, Cambridge, Massachusetts 02139, United States

<sup>§</sup>Diamond Nanotechnologies, Inc., Boston, Massachusetts 02134, United States

## S Supporting Information

**ABSTRACT:** Numerous theoretical protocols have been developed for quantum information processing with dipole-coupled solid-state spins. Nitrogen vacancy (NV) centers in diamond have many of the desired properties, but a central challenge has been the positioning of NV centers at the nanometer scale that would allow for efficient and consistent dipolar couplings. Here we demonstrate a method for chip-scale fabrication of arrays of single NV centers with record spatial localization of about 10 nm in all three dimensions and controllable inter-NV spacing as small as 40 nm, which approaches the length scale of strong dipolar coupling. Our approach uses masked implantation of nitrogen through nanoapertures in a thin gold film, patterned via electron-beam lithography and dry etching. We verified the position and spin properties of the resulting NVs through wide-field super-resolution optically detected magnetic resonance imaging.

**KEYWORDS:** Nanopatterning, quantum computing, single spin, nitrogen vacancy, diamond, ion implantation



Optically addressable spin systems in solids, such as quantum dots<sup>1–3</sup> and atomic crystal impurities,<sup>4–9</sup> are currently the subject of considerable interest for their potential as spin qubits for quantum information processing<sup>10–12</sup> and sensors of magnetic field and temperature with nanometer spatial resolution.<sup>13–16</sup> The negatively charged nitrogen-vacancy (NV) center in diamond<sup>17</sup> has become a leading candidate for the implementation of a solid state quantum processor that can function at ambient conditions. Its optically addressable electron spin state can be initiated and measured with high fidelity and coherently controlled through microwave pulses,<sup>18</sup> thanks to its excellent photostability and millisecond coherence time at room temperature<sup>19</sup> (reaching 1 s at 77 K)<sup>20</sup> in ultrapure, isotopically engineered diamond. These unique features have enabled important recent accomplishments, including high-fidelity one- and two-qubit gates,<sup>21</sup> electron-spin based quantum registers,<sup>22</sup> entanglement between two NV centers via dipolar coupling,<sup>8</sup> and long-distance heralded entanglement mediated by photons.<sup>23</sup>

Central to many quantum information processing applications with NV centers is the ability to produce small clusters of magnetically coupled spins. Two exemplary applications are (i) error-corrected quantum registers<sup>24</sup> that could serve as memories in modular quantum computers<sup>25</sup> and quantum repeater networks<sup>26,27</sup> and (ii) room-temperature quantum computing.<sup>28–30</sup> (i) Limited error correction was already

demonstrated with three nuclear spins coupled via the NV's electron spin system<sup>31</sup> but general error correction requires at least nine spins, a number that becomes difficult and slow to control with only one NV electron spin. One promising solution is to increase the number of NVs per error-corrected quantum register to  $\sim 3$  or more, which is feasible as long as NVs are within  $\sim 10$  nm from each other to allow fast ( $\sim$ tens of kilohertz) dipolar coupling. (ii) Although room-temperature quantum computing approaches have been shown to tolerate some randomness in spin-spacing and hence dipolar coupling strength, consistent coupling achieves highest performance.

A common requirement for all of these applications is that the mutual dipolar interaction of two neighboring NV spins be larger than the coupling of each individual spin with the surrounding environment. Given demonstrated coherence times of  $\sim 1$  ms and the rapid  $r^{-3}$  decay of the dipole–dipole interaction with separation,<sup>22</sup> NVs must be colocalized to within  $\sim 40$  nm while preserving optimal spin quality. More precise positioning directly translates into higher theoretical two-qubit entanglement fidelities, as well as tolerance for environmental decoherence. The scalable creation of high-

Received: April 26, 2016

Revised: July 12, 2016

Published: July 18, 2016



quality NV centers with nanometer-scale positioning accuracy is therefore a central challenge for these approaches.

Various methods to engineer NV centers through  $^{15}\text{N}^+$  ion implantation and annealing have been pursued. Serial implantation techniques, using maskless focused ion beam<sup>32–34</sup> or pierced scanning probe,<sup>35,36</sup> are flexible methods for the creation of individual NV centers in predetermined locations (for focused ion beam) or the technique is not easily scalable to large areas (for the pierced AFM). Therefore, parallel implantation employing lithographically defined masks has been developed to simultaneously address the requirement of placement accuracy and high throughput. Examples of such masks include apertures in PMMA<sup>37–39</sup> (diameter >30 nm), high-aspect-ratio nanochannels in mica<sup>40</sup> (diameter >30 nm, randomly positioned), and sub-10 nm linear trenches in silicon.<sup>41</sup> The latter represents the highest lateral resolution demonstrated to date but suffers from limited site-to-site pitch and low localization in the axial direction. To obtain a spatial distribution of implanted NV centers with small fwhm and simultaneously guarantee a high implantation isolation outside of the defined apertures, masks made with low density and low atomic weight materials must be thick, that is, on the scale of hundreds of nanometers. However, thick masks do not allow closely spaced patterns.

In this work, we present a fabrication technique for creating arrays of shallow NV centers with  $\sim 10$  nm spatial localization and site-to-site spacing of 40 nm, as illustrated in Figure 1. This

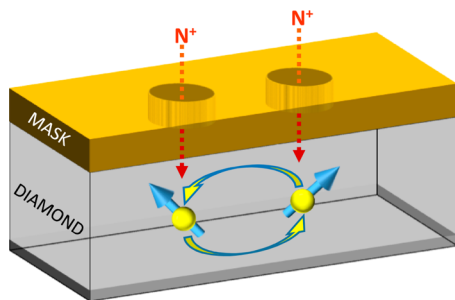


**Figure 1.** Concept for the creation of closely spaced electronic spins in diamond. The implantation of nitrogen through a mask presenting nanoscale apertures in close proximity to one another, enables the creation of NV centers with high spatial resolution and fine pitch. This allows the possibility of entanglement of adjacent spin qubits by means of direct magnetic dipole coupling.

pitch is sufficiently small for magnetic dipole coupling between NVs implanted through neighboring apertures to be faster than decoherence processes for NVs with demonstrated millisecond  $T_2$  times<sup>8</sup> that in principle allow for dipole-mediated entanglement. Our process relied on high resolution electron-beam lithography in combination with dry etching to create apertures in a 35 nm thick gold film deposited directly onto an ultrapure CVD-grown diamond substrate. This was subsequently irradiated with high energy  $^{15}\text{N}^+$  ions and annealed to form  $\text{NV}^-$  centers. We imaged the resulting color centers via super-resolution microscopy and characterized their optically addressable spins. The high atomic mass and high density mask ensures excellent implantation isolation (more than 40 dB) that permits the formation of nanoscale apertures with low aspect-ratio and close spacing, achieving high spatial resolution and fine pitch across the diamond sample.

The fabrication process is illustrated in Figure 2 (for details, see the Methods section). We deposited 8 nm of Cr and 35 nm of Au

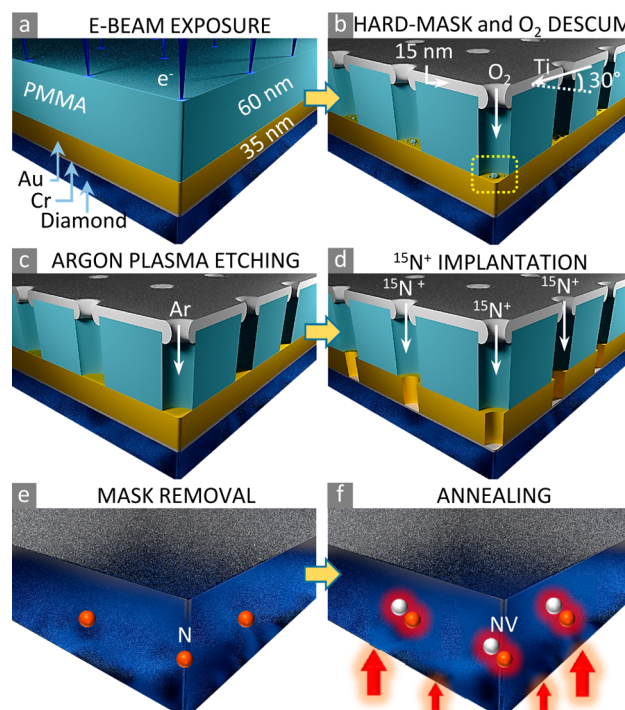


**Figure 2.** Fabrication process schematics. (a) A bulk diamond substrate was masked by depositing 8 nm of Cr and 35 nm of Au. Electron beam lithography was used to pattern a 60 nm thick PMMA film. (b) Titanium was deposited at a 30° angle with the substrate to form a hard-mask on the surface of the developed resist. O<sub>2</sub> RIE was applied to eliminate eventual resist residue. (c) Pattern transfer to the underlying metal mask was achieved by means of RIE with argon. (d) Broad-beam implantation of  $^{15}\text{N}^+$  ions at 10 keV resulted in the insertion of substitutional nitrogen within the diamond lattice, approximately 10 nm below the surface. (e) The resist and the metal mask were removed with wet chemical treatments. (f) Annealing the sample at 1000 °C allowed the formation of NV centers.

adhesion layer and 35 nm of Au by electron beam evaporation on a high-purity synthetic diamond substrate (Element Six, [N] < 5 ppb, [ $^{13}\text{C}$ ] = 1.1%). Electron beam lithography (using a Nanobeam nB4 lithography system) was used to pattern apertures in a 60 nm thick PMMA film spin-coated onto the gold layer (Figure 2a). After development of the resist, samples were coated with a 15 nm thick Ti hard-mask deposited at 30° angle to the surface as shown in Figure 2b. This angular deposition method decreased the diameter of the apertures while protecting the top surface of the resist during the oxygen plasma reactive ion etching (RIE), used to remove any resist residue from the bottom of the apertures. We transferred the pattern to the Au layer using anisotropic ICP etching with argon plasma (Figure 2c). Because the thickness of the oxidized metal-protected resist was twice that of the Au layer, the aperture pattern could be transferred without jeopardizing the integrity of the mask. Note that the underlying Cr layer was not etched to protect the diamond surface from plasma-induced damage and to reduce the likelihood of ion channeling during implantation.<sup>37,39,41,42</sup>

Figure 3a–c shows SEM micrographs of 40 nm-pitch aperture arrays in the mask with diameter of approximately 10 nm at various stages in the fabrication process. Before

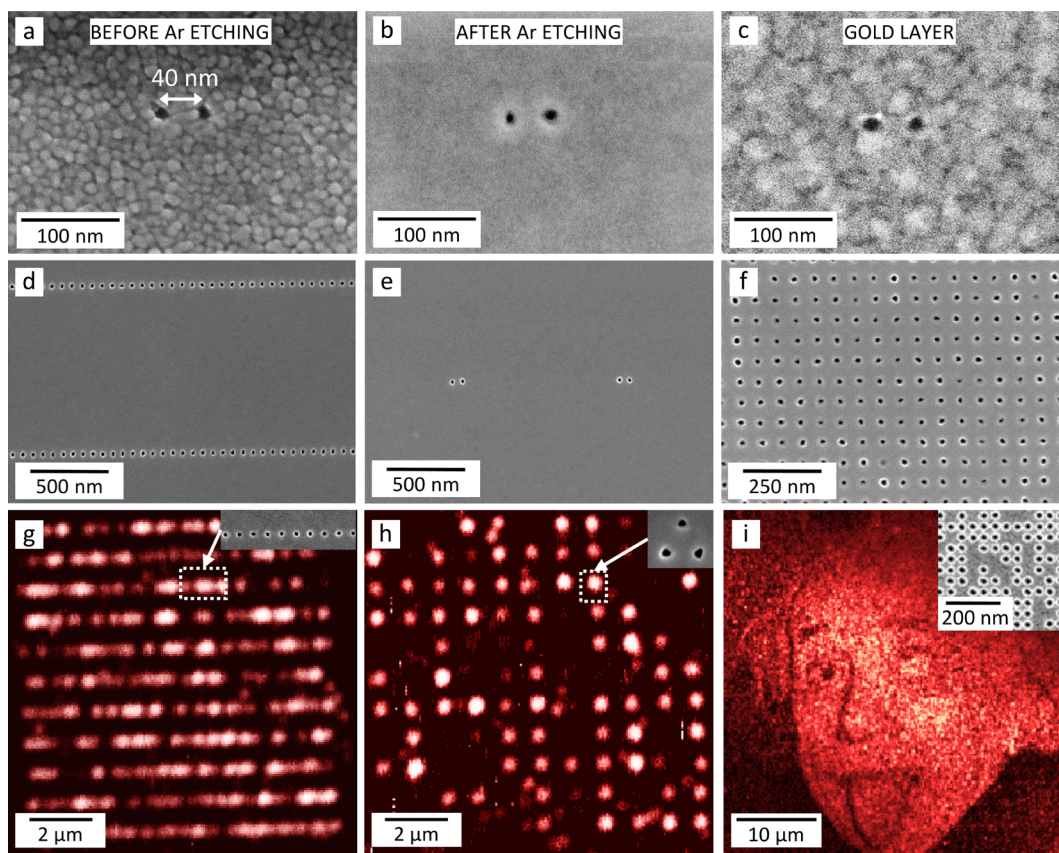


**Figure 3.** SEM micrographs of the masks. (a) Top-view image after the deposition of a 15 nm thick Ti hard-mask by angled e-beam evaporation. Representative cluster composed of a pair of circular apertures with 40 nm pitch and approximately 15 nm diameter. The metal reduces the diameter of the circular features in the PMMA. The grain size is clearly visible (approximately 10 nm) and introduces edge roughness along the rim of the apertures. (b) After argon RIE, the Ti surface is smoother and the grains are no longer visible. The diameter of the circular apertures is also reduced. (c) The resulting Au layer shows clear pattern transfer. Examples of different configurations of circular features constituting the mask design: (d) chains, (e) pairs, and (f) 2D arrays. (g–i) Scanning confocal fluorescence micrographs of NV centers in diamond after masked implantation and annealing. The bright spots in the images derive from the NV center PL, and reproduces the design of the mask (shown in the insets) for arrays (1  $\mu\text{m}$  spacing) of 60 nm pitch (g) chains, (h) triangular clusters, (i) and a grayscale photograph with 40 nm pitch apertures (original photo by ullstein bild/ullstein bild via Getty Images, reproduced with permission).

applying the Ar plasma, the Ti hard-mask coating the resist presented the granular structure typical of thin films deposited by e-beam evaporation, which introduces an apparent edge-roughness along the rim of the holes in PMMA, which otherwise are circular with smooth edges. Following the pattern transfer with Ar etching, the top surface of the mask appeared smooth due to the sputtering action of the  $\text{Ar}^+$  ions, and the diameter of the apertures in the resist was reduced, possibly because of structural changes in the heavily cross-linked polymer during exposure to the Ar plasma. To confirm the pattern transfer to the Au mask, we removed the PMMA layer from a test sample and imaged the gold surface directly, observing apertures as defined by the e-beam patterned PMMA (Figure 3c). We created a mask containing arrays of apertures with various configurations to demonstrate the flexibility of this high-throughput approach for the precise positioning of NV centers. Figure 3d–f displays linear chains, isolated pairs and two-dimensional arrays of 60 nm pitch apertures in a mask with lateral cross-section as sketched in Figure 2d. The diameter of the circular features was varied between 10 and 20 nm by controlling the e-beam dose to allow separations as small as 20 nm between neighboring apertures in the case of 40 nm pitch arrays.

Following mask fabrication, the broad-beam implantation of 10 keV  $^{15}\text{N}^+$  ions (carried out by INNOViON Corp.) introduced shallow nitrogen atoms at the predicted depth of 7.5 nm below the diamond surface at the location of the mask apertures, as illustrated in Figure 2d. The isolation provided by the multilayered mask prevents ion implantation in correspondence with masked regions with >99.98% probability (details of the ion implantation are supplied in Methods; SRIM simulations<sup>43</sup> are presented in Supporting Figure S1). NVs implanted within the same aperture have a predicted mean spacing of 12 nm in three dimensions (see Supporting Figure S2), enabling entanglement between collocated NVs within a coherence time of the order  $T_2 \sim 50 \mu\text{s}$ . After the implantation, we removed the mask and annealed the sample at 1000  $^\circ\text{C}$  to mobilize lattice vacancies, allowing them to be captured by substitutional nitrogen atoms, thus forming NV centers<sup>44,45</sup> while at the same time repairing lattice damage (Figure 2e,f). We performed a final acid treatment and surface termination with oxygen to increase the yield of formation of negatively charged  $\text{NV}^-$  versus neutral  $\text{NV}^0$  centers as well as their photostability.<sup>41,46–48</sup>

We imaged the NV spin arrays via scanning confocal fluorescence microscopy using an oil immersion objective (NA = 1.3) and excitation by a 532 nm continuous wave laser (see

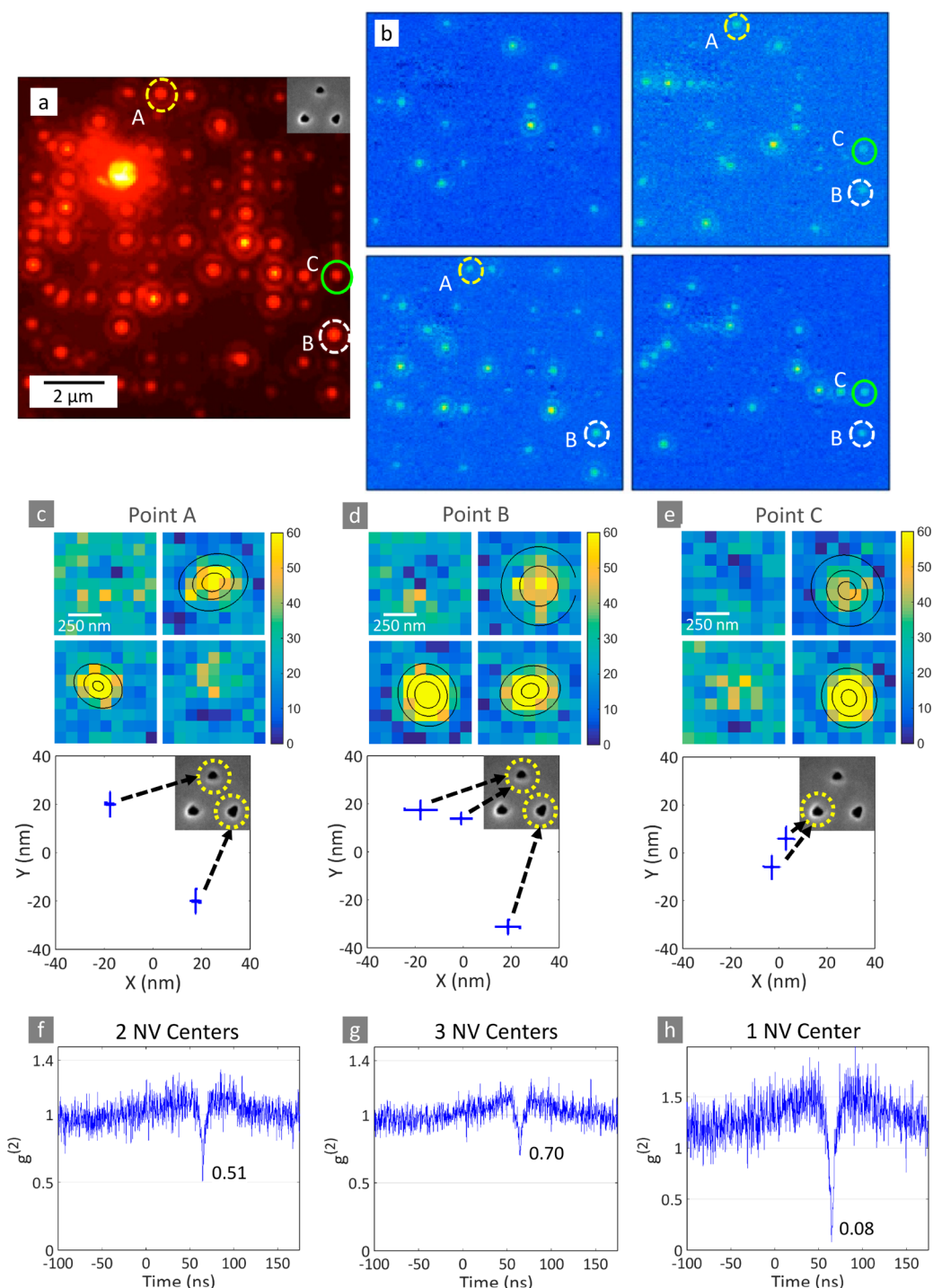


**Figure 4.** NV localization via super-resolution microscopy. (a) Wide-field image of the PL of NV centers created via implantation through a mask presenting triangular arrays of 60 nm pitch circular apertures (shown in the inset). Three representative sites (circled and labeled A, B, and C) were further analyzed with super-resolution microscopy. (b) Four-quadrant contrast ESR image of the same region for four microwave resonances corresponding with the different crystal orientations of the NV centers. A decrease in PL intensity upon application of a microwave is indication of the presence of at least one NV center in the selected orientation and is represented in the image by a bright spot. (c–e) Super-resolution imaging of NV positions at the three selected sites. Gaussian fit of the contrast ESR signal (above) and reconstruction of the NV locations within the triangular cluster (below) for (c) point A, (d) point B, and (e) point C. Error bars correspond to the 95% confidence interval of the Gaussian fit. (f–h) Second order autocorrelation function of NV PL allowed the estimation of the number of NV centers present in a cluster, indicating (f) 2 NV centers if  $0.5 < g^{(2)}(0) < 0.66$ , (g) 3 NV centers if  $0.66 < g^{(2)}(0) < 0.75$ , and (h) a single NV if  $g^{(2)}(0) < 0.5$ .

Methods for details) as shown in Figure 3g–i. The bright dots in the scans correspond to NV center photoluminescence (PL), and the relative brightness varies according to the number of NVs per cluster. From the observed number of nonfluorescing

array sites, we estimated a Poisson parameter  $\lambda = 0.5$  NVs per 15 nm diameter aperture, corresponding to a  $^{15}\text{N}^+$  to NV implantation yield of approximately 2.7%. Additionally, we estimated a mask isolation of 41 dB from the ratio of on-site to

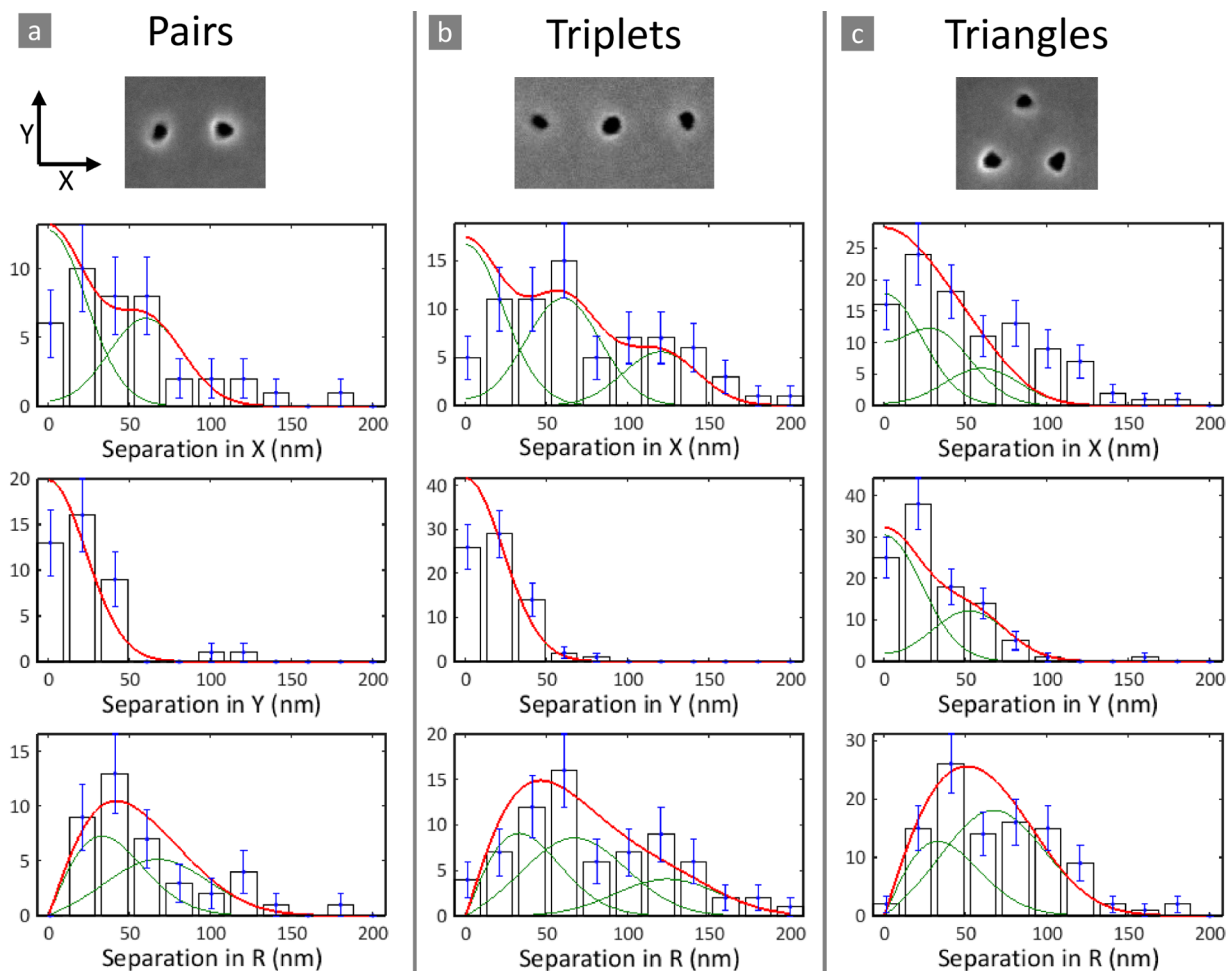


**Figure 5.** Statistics of NV–NV spacing. (a) Forty-one pairwise NV–NV separations resulting from linearly paired apertures with 60 nm pitch, (b) 80 from linear triplets, and (c) 106 from triangles (the mask is shown in the SEM images). The green curves are the predicted pairwise NV–NV spacing distributions for each two-aperture pair (including combinatorial weights), derived from the Chi distribution with one ( $X$ ,  $Y$ ) and two ( $R$ ) degrees of freedom, and the red curve is the overall predicted distribution for shown aperture configuration.

off-site NV density (see [Supporting Information](#) and [Figure S3](#) for details of the calculation). This estimate of the isolation is lower than the simulated limit, possibly due to modifications of the resist layer during the argon plasma etching and to the polycrystalline nature of the metallic mask resulting in a reduction of effective thickness at grain boundaries. Large-scale arbitrary patterning is also possible. We demonstrated this by creating a reproduction of a photograph on the mask varying the density of 15 nm apertures with 40 nm pitch to achieve a grayscale image. The scanning confocal fluorescence micrograph of the resulting NVs after implantation through the grayscale image on the mask is shown in [Figure 3i](#).

To measure the precision in placement of the NV arrays, we employed wide-field super-resolution localization through optically detected magnetic resonance (ODMR)<sup>41,49</sup> (see [Methods](#) for details). This technique allows for localization of NVs within each of the four distinct geometric classes available in single-crystal diamond, corresponding to the four possible (111) crystallographic orientations, by sequentially driving each class into a low-fluorescence “dark” state. A representative measurement of an array of triangularly arranged NV centers is shown in [Figure 4](#). We measured the photoluminescence intensity of the array without microwave drive ([Figure 4a](#)), as well as under continuous-wave driving on resonance with NVs

in each of the four geometric classes (resonance profile presented in [Supporting Figure S4](#)). The difference between the off-resonance and on-resonance PL intensities ([Figure 4b](#)) isolates the signal originating from NV centers associated with each particular orientation, which we then fitted with a 2D Gaussian curve ([Figure 4c–e](#)) to determine the position of each NV below the diffraction limit. In this example, we identified three different NV configurations, corresponding to NV centers implanted through different apertures with a minimum lateral spacing of  $13 \pm 5$  nm for two NVs observed in [Figure 4e](#). Finally, as this super-resolution method cannot distinguish between two NVs in the same geometric class, we confirmed the NV number through second-order photon correlation measurements, as shown in [Figure 4f,g](#), with [Figure 4i](#) presenting a single-NV photon antibunching curve for reference.

To demonstrate that we have nanoscale control over the position of the engineered NVs, we repeated these wide-field super-resolution measurements across several arrays consisting of apertures configured in pairs, linear triplets, and triangular arrangements with 60 nm pitch. We identified approximately 200 sites containing more than one NV. For each, we computed the NV–NV spacing of all independent pairings (227 pairings in total). The resulting frequency histograms are

shown in Figure 5. The pairs and linear triplets have characteristic peaks at about zero and 60 nm separation in the  $X$  direction, associated with NVs implanted through the same and neighboring apertures respectively, while the linear triplets also have a peak at 120 nm associated with NVs implanted through apertures at opposing ends. For both arrangements, the distribution in the  $Y$  direction is centered at zero with no features elsewhere. In contrast, the triangular configuration results in a significantly different profile with characteristic peaks prominently occurring at  $Y = 51$  nm, reflecting the presence of the vertically displaced aperture. In total displacement  $R$ , the linear triplets display a long tail toward 150 nm, while the pairs and triangles are more tightly spaced. We modeled the expected outcomes using the Chi distribution with one ( $X, Y$ ) and two ( $R$ ) degrees of freedom, as shown in the solid curves in Figure 5. The variance of the distribution reflects the combination of several sources of broadening, including the width of the implantation aperture, the implantation straggle, and the super-resolution measurement error, while each possible pairwise aperture combination is treated as a separate distribution with a mean determined by the aperture spacing for that combination. We considered the combinatorial weights of each population (green curves) and summed them to create a predicted NV–NV spacing model (red curves), which agrees with the experimental data. In fact, it reproduces the characteristic features of triplets and triangles in  $X$  and  $Y$  respectively, showing that NVs created with this technique are indeed controllably patterned at the nanoscale.

Finally, we characterized the coherent spin properties of the implanted NVs using wide-field pulsed ODMR at ambient conditions. We performed Hahn spin–echo and CPMG- $N$  sequences for pulse number  $N = 2, 4, 8, 16, 32, 64$  on the implanted NV arrays with the averages across the array shown in Figure 6. The array-average coherence time  $T_{2, \text{echo}} = 10 \mu\text{s}$  was increased to  $T_{2, \text{CPMG-64}} = 67 \mu\text{s}$  through higher order decoupling with a fitted relation  $T_{2, \text{CPMG-}N} = aN^2$  describing the NV performance scaling with increased pulse number. The NV coherence times reached here are comparable to shallow-implanted NVs<sup>16,50,51</sup> and are sufficient for the coherent manipulation of entangled NV spins separated by up to 20 nm.

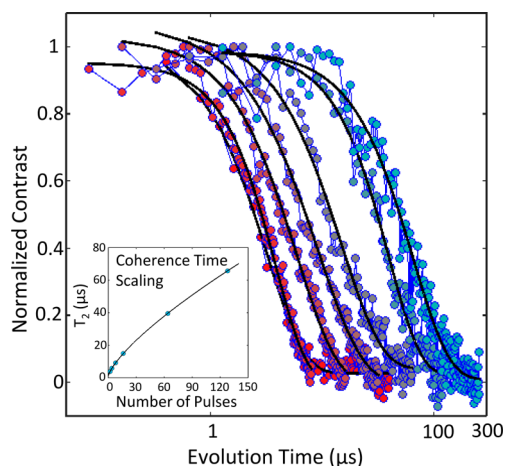


**Figure 6.** Coherence time extension via CPMG. The coherence time of engineered NVs is increased by means of CPMG- $N$  pulse sequences for  $N = 2, 4, 8, 16, 64, 128$  from left to right. Black lines: fits to  $Ae^{-(t/t_2)^x}$ . Inset: Scaling of extracted  $T_2$  time with number of decoupling pulses.

A likely source of decoherence in this sample is constituted by proximal surface spins, which recently have been shown to dominate the magnetic noise spectrum at depths similar to the nominal 7.5 nm implant of this sample.<sup>52,53</sup> Arrays implanted with a lower  $^{15}\text{N}^+$  fluency ( $10^{12}$  ions/ $\text{cm}^2$ ,  $10\times$  reduced) show similar spin coherence times (see Supporting Figure S5), indicating that implanted nuclear and electronic dark spins are not the dominant source of decoherence.

To further decrease the decoherence rate to match the mask-defined coupling strength at separations of 40 nm, a reduction of the magnetic noise is needed. This could be achieved by increasing the mask thickness, allowing for a deeper implant but with expected increase in straggle and poorer localization. Alternatively, different surface terminations such as overgrown diamond,<sup>54</sup> nitrogen reconstruction,<sup>55</sup> or high-dielectric constant materials<sup>56,57</sup> could be used while maintaining a shallow implantation depth. Though the contribution of surface electron spins is likely dominant, eliminating the  $^{13}\text{C}$  nuclear spin bath through isotopic purification<sup>19</sup> could also increase coherence times in these shallow-implanted spin arrays.

Beyond increasing the coherence time of implanted NVs via elimination of electric and magnetic noise sources, the fabricated spin arrays have several avenues of further improvement. The single-aperture NV yield of 0.5 reflects an N to NV conversion yield of only 2.7%. This could be improved by repeated coimplantation,<sup>58</sup> which could increase the NV<sup>-</sup> formation yield to 25%. In turn, this would allow for significant reduction in implantation dose, simultaneously reducing noise<sup>59</sup> while increasing the probability of multi-NV sites. If surface issues are resolved, allowing for even shallower implant with comparable or better spin coherence times, the mask thickness could be reduced and aperture pitch could be decreased toward the limit of electron beam lithography,<sup>60,61</sup> as shown in Supporting Figure S6 for a pair of apertures with 20 nm pitch. Likewise, roughness introduced by finite grain size of the metal could be overcome through the use of single-crystal metallic masks, either by improving the deposition<sup>62</sup> or transfer of chemically synthesized membranes.

The current fabrication methodology already allows for the production of millions of implantation apertures in arbitrary patterns, which could enable the development of solid-state spin arrays or spin chains on the length scale of dipole-mediated spin diffusion. The engineering of near-surface NV centers could also become central to many sensing applications, in which the distance of the NV sensor to the object of interest must be controlled with nanometer precision. Furthermore, the resulting NV arrays could be integrated with nanophotonic, plasmonic and electronic devices by performing subsequent aligned processes using etched registration marks created concurrently with the fabrication of the mask, paving the way for the development of a quantum network. Finally, the NV quantum registers themselves can be extended by implanting into a  $^{13}\text{C}$ -enriched layer, so that multiple nuclear spins can be addressed by means of individual NV center and error correction can be implemented within each site.<sup>31,63</sup>

**Methods. Fabrication of the Nanopatterned Mask.** The small diamond substrate was mounted onto a carrier silicon chip and by means of electron-beam evaporation (Angstrom EvoVac) performed at a rate of  $0.5 \text{ \AA/s}$  while maintaining the chamber pressure below  $5 \times 10^{-7}$  mbar, a thin film of 8 nm of Cr and 35 nm of Au was created. An indium wire was then used to establish an electrical connection between the top surface of the gold-coated diamond sample and the carrier silicon chip, as

required during electron-beam lithography. Next, the chip carrying the diamond was attached onto a glass coverslip and mounted off-center on a spinner, to increase the tangential velocity and avoid the accumulation of resist at the corners of the 2 mm × 2 mm diamond, observed in the case of centered spin-coating. Poly(methyl methacrylate) (PMMA) of molecular weight 495 K (2% solution in anisole) was spun to create a 60 nm thick film and baked at 180 °C for 15 min. The electron-beam exposure (Nanobeam nB4 lithography system) was performed using 80 kV accelerating voltage, current 400 pA, varying the dose between 1500 and 3600  $\mu\text{C}/\text{cm}^2$ . The layout contained different arrangements (singles, pairs, triplets, triangles, linear chains, 2D arrays) of 40 and 60 nm pitch ensembles of circles, covering the whole surface of the sample. The resist was developed for 60 s in a solution of methyl-isobutyl ketone/isopropanol (MIBK/IPA, 1:3 by volume) at 5 °C, applying ultrasonic agitation for increased resolution and contrast, and rinsed in IPA to stop the development. The chip was mounted on a 60° inclined support (with respect to the vertical) to perform a tilted deposition of a 15 nm thick Ti film by means of electron-beam evaporation (Semicore S-2000), forming a protective hard mask. The samples underwent a 10 s oxygen plasma treatment (Diener Tetra 30 PC plasma cleaner, 0.25 mbar, 4 sccm O<sub>2</sub> flow, 212 V DC bias, 300 W RF power at 13.56 MHz) meant to eliminate residual resist from within the developed features. The pattern transfer to the gold layer was accomplished by means of an argon plasma, applied for a total of 6 min (Oxford PlasmaLab 80 Plus ICP 6S, 60 W forward power, 0 W ICP power, 50 sccm of Ar repeated 18 times for 20 s each, spaced by 30 s Ar flushing).

**Ion Implantation, Annealing, and Surface Passivation.** The sample was implanted (INNOVION Corp.) with 10 keV <sup>15</sup>N<sup>+</sup> ions at an angle of 6° from the perpendicular to the surface (100) to decrease ion channeling<sup>38,45</sup> and with fluencies ranging from 10<sup>10</sup> to 10<sup>13</sup> ions/cm<sup>2</sup>. We then removed the mask using solvents and acids (acetone to remove the resist, KI/I<sub>2</sub> gold etchant, CR7 chrome etchant, dilute HF to remove titanium). To promote vacancy diffusion and the formation of NV centers with the implanted interstitial nitrogen atom, we annealed the sample at 850 °C in a vacuum furnace for 2 h. During the annealing process, the surface of the diamond sample develops graphitic carbon impurities that we removed by immersion in a mixture of perchloric, sulfuric, and nitric acid (1:1:1), which does not attack the diamond sp<sup>3</sup> bonds. An additional annealing step at 1000 °C in a high vacuum furnace (<10<sup>-6</sup> mbar) was performed to increase the NV<sup>-</sup> formation yield and its electron spin coherence time.<sup>45</sup> Finally, the diamond was baked at 475 °C in a dry 30% O<sub>2</sub> atmosphere for 2 h to achieve oxygen surface termination.<sup>46</sup>

**Photoluminescence and ODMR Measurements.** The PL measurements were performed on a custom-made fluorescence microscope. Optical excitation illumination was provided by a 532 nm laser either focused on the back focal plane of the objective for wide-field illumination or collimated for confocal operation. The emitted NV fluorescence was collected using an oil-immersion objective with NA = 1.3, separated from the excitation beam path through a dichroic mirror, spectrally filtered with a 635 nm long-pass filter, and directed either onto an EMCCD for wide-field measurements or into single mode fiber for single-photon detection. Resonant microwaves were applied to the sample through a 15  $\mu\text{m}$  wide copper wire positioned on the diamond surface within  $\sim 20$   $\mu\text{m}$  from the measured NVs.

## ■ ASSOCIATED CONTENT

### 📄 Supporting Information

The Supporting Information is available free of charge on the ACS Publications website at DOI: 10.1021/acs.nanolett.6b01692.

NV–NV separation modeling; conversion yield and isolation estimation; optically detected magnetic resonance spectrum; spin measurements at lower implantation dose; mask patterning resolution limits(PDF)

## ■ AUTHOR INFORMATION

### Corresponding Authors

\*E-mail: (S.W.) [sw2128@columbia.edu](mailto:sw2128@columbia.edu).

\*E-mail: (D.E.) [englund@mit.edu](mailto:englund@mit.edu).

### Author Contributions

D.S. fabricated the implantation mask and contributed to the super-resolution measurements. M.T. performed the post-implantation processing, super-resolution measurements, and spin coherence characterization. D.S. and M.T. drafted the paper. All authors participated in conceiving the experiment, discussed the results, and commented on the manuscript. D.S. and M.T. contributed equally.

### Notes

The authors declare no competing financial interest.

## ■ ACKNOWLEDGMENTS

The authors would like to thank C. Forsythe, E. Chen, H. Cai, and F. Dolde for helpful discussions. This work was supported in part by the Air Force Office of Scientific Research (AFOSR) Multidisciplinary University Research Initiative (FA9550-14-1-0052) “Optimal Measurements for Scalable Quantum Technologies”, the AFOSR PECASE (directed by Dr. Gernot Pomrenke), and the Defense Threat Reduction Agency Basic Research Award #HDTRA1-11-1-0022 to Columbia University. Fabrication and processing at Columbia were performed in the CEPSR Cleanroom under the auspices of the Columbia Nanoscience Initiative.

## ■ REFERENCES

- (1) De Greve, K.; Yu, L.; McMahon, P. L.; Pelc, J. S.; Natarajan, C. M.; Kim, N. Y.; Abe, E.; Maier, S.; Schneider, C.; Kamp, M.; Hofling, S.; Hadfield, R. H.; Forchel, A.; Fejer, M. M.; Yamamoto, Y. *Nature* **2012**, *491* (7424), 421–5.
- (2) Gao, W. B.; Fallahi, P.; Togan, E.; Delteil, A.; Chin, Y. S.; Miguel-Sanchez, J.; Imamoglu, A. *Nat. Commun.* **2013**, *4*, 2744.
- (3) Schaibley, J. R.; Burgers, A. P.; McCracken, G. A.; Duan, L. M.; Berman, P. R.; Steel, D. G.; Bracker, A. S.; Gammon, D.; Sham, L. J. *Phys. Rev. Lett.* **2013**, *110* (16), 167401.
- (4) Morton, J. J. L.; Tyryshkin, A. M.; Brown, R. M.; Shankar, S.; Lovett, B. W.; Ardavan, A.; Schenkel, T.; Haller, E. E.; Ager, J. W.; Lyon, S. A. *Nature* **2008**, *455* (7216), 1085–1088.
- (5) Simmons, S.; Brown, R. M.; Riemann, H.; Abrosimov, N. V.; Becker, P.; Pohl, H. J.; Thewalt, M. L.; Itoh, K. M.; Morton, J. J. *Nature* **2011**, *470* (7332), 69–72.
- (6) Muller, T.; Hepp, C.; Pingault, B.; Neu, E.; Gsell, S.; Schreck, M.; Sternschulte, H.; Steinmuller-Nethl, D.; Becher, C.; Atature, M. *Nat. Commun.* **2014**, *5*, 3328.
- (7) Hanson, R.; Mendoza, F. M.; Epstein, R. J.; Awschalom, D. D. *Phys. Rev. Lett.* **2006**, *97* (8), 087601.
- (8) Dolde, F.; Jakobi, I.; Naydenov, B.; Zhao, N.; Pezzagna, S.; Trautmann, C.; Meijer, J.; Neumann, P.; Jelezko, F.; Wrachtrup, J. *Nat. Phys.* **2013**, *9* (3), 139–143.
- (9) Widmann, M.; Lee, S. Y.; Rendler, T.; Son, N. T.; Fedder, H.; Paik, S.; Yang, L. P.; Zhao, N.; Yang, S.; Booker, I.; Denisenko, A.;

- Jamali, M.; Momenzadeh, S. A.; Gerhardt, I.; Ohshima, T.; Gali, A.; Janzen, E.; Wrachtrup, J. *Nat. Mater.* **2014**, *14* (2), 164–8.
- (10) Hanson, R.; Awschalom, D. D. *Nature* **2008**, *453* (7198), 1043–9.
- (11) Gao, W. B.; Imamoglu, A.; Bernien, H.; Hanson, R. *Nat. Photonics* **2015**, *9* (6), 363–373.
- (12) Awschalom, D. D.; Bassett, L. C.; Dzurak, A. S.; Hu, E. L.; Petta, J. R. *Science* **2013**, *339* (6124), 1174–1179.
- (13) Maze, J. R.; Stanwix, P. L.; Hodges, J. S.; Hong, S.; Taylor, J. M.; Cappellaro, P.; Jiang, L.; Dutt, M. V.; Togan, E.; Zibrov, A. S.; Yacoby, A.; Walsworth, R. L.; Lukin, M. D. *Nature* **2008**, *455* (7213), 644–7.
- (14) Balasubramanian, G.; Chan, I. Y.; Kolesov, R.; Al-Hmoud, M.; Tisler, J.; Shin, C.; Kim, C.; Wojcik, A.; Hemmer, P. R.; Krueger, A.; Hanke, T.; Leitenstorfer, A.; Bratschitsch, R.; Jelezko, F.; Wrachtrup, J. *Nature* **2008**, *455* (7213), 648–51.
- (15) Mamin, H. J.; Kim, M.; Sherwood, M. H.; Rettner, C. T.; Ohno, K.; Awschalom, D. D.; Rugar, D. *Science* **2013**, *339* (6119), 557–560.
- (16) Simin, D.; Fuchs, F.; Kraus, H.; Sperlich, A.; Baranov, P. G.; Astakhov, G. V.; Dyakonov, V. *Phys. Rev. Appl.* **2015**, *4* (1), 014009.
- (17) Doherty, M. W.; Manson, N. B.; Delaney, P.; Jelezko, F.; Wrachtrup, J.; Hollenberg, L. C. L. *Phys. Rep.* **2013**, *528* (1), 1–45.
- (18) Jelezko, F.; Wrachtrup, J. *Phys. Status Solidi A* **2006**, *203* (13), 3207–3225.
- (19) Balasubramanian, G.; Neumann, P.; Twitchen, D.; Markham, M.; Kolesov, R.; Mizuochi, N.; Isoya, J.; Achard, J.; Beck, J.; Tisler, J.; Jacques, V.; Hemmer, P. R.; Jelezko, F.; Wrachtrup, J. *Nat. Mater.* **2009**, *8* (5), 383–7.
- (20) Bar-Gill, N.; Pham, L. M.; Jarmola, A.; Budker, D.; Walsworth, R. L. *Nat. Commun.* **2013**, *4*, 1743.
- (21) Rong, X.; Geng, J.; Shi, F.; Liu, Y.; Xu, K.; Ma, W.; Kong, F.; Jiang, Z.; Wu, Y.; Du, J. *Nat. Commun.* **2015**, *6*, 8748.
- (22) Neumann, P.; Kolesov, R.; Naydenov, B.; Beck, J.; Rempp, F.; Steiner, M.; Jacques, V.; Balasubramanian, G.; Markham, M. L.; Twitchen, D. J.; Pezzagna, S.; Meijer, J.; Twamley, J.; Jelezko, F.; Wrachtrup, J. *Nat. Phys.* **2010**, *6* (4), 249–253.
- (23) Pfaff, W.; Hensen, B. J.; Bernien, H.; van Dam, S. B.; Blok, M. S.; Taminiu, T. H.; Tiggelman, M. J.; Schouten, R. N.; Markham, M.; Twitchen, D. J.; Hanson, R. *Science* **2014**, *345* (6196), 532–535.
- (24) Cramer, J.; Kalb, N.; Rol, M. A.; Hensen, B.; Blok, M. S.; Markham, M.; Twitchen, D. J.; Hanson, R.; Taminiu, T. H. 2015, arXiv:1508.01388.
- (25) Nickerson, N. H.; Fitzsimons, J. F.; Benjamin, S. C. *Phys. Rev. X* **2014**, *4* (4), 041041.
- (26) Barrett, S. D.; Kok, P. *Phys. Rev. A: At, Mol., Opt. Phys.* **2005**, *71* (6), 060310.
- (27) Childress, L.; Taylor, J. M.; Sorensen, A. S.; Lukin, M. D. *Phys. Rev. A: At, Mol., Opt. Phys.* **2005**, *72* (5), 052330.
- (28) Yao, N. Y.; Jiang, L.; Gorshkov, A. V.; Maurer, P. C.; Giedke, G.; Cirac, J. I.; Lukin, M. D. *Nat. Commun.* **2012**, *3*, 800.
- (29) Ping, Y.; Lovett, B. W.; Benjamin, S. C.; Gauger, E. M. *Phys. Rev. Lett.* **2013**, *110* (10), 100503.
- (30) Cai, J.; Retzker, A.; Jelezko, F.; Plenio, M. B. *Nat. Phys.* **2013**, *9* (3), 168–173.
- (31) Taminiu, T. H.; Cramer, J.; van der Sar, T.; Dobrovitski, V. V.; Hanson, R. *Nat. Nanotechnol.* **2014**, *9* (3), 171–6.
- (32) Meijer, J.; Burchard, B.; Domhan, M.; Wittmann, C.; Gaebel, T.; Popa, I.; Jelezko, F.; Wrachtrup, J. *Appl. Phys. Lett.* **2005**, *87* (26), 261909.
- (33) Rabeau, J. R.; Reichart, P.; Tamanyan, G.; Jamieson, D. N.; Praver, S.; Jelezko, F.; Gaebel, T.; Popa, I.; Domhan, M.; Wrachtrup, J. *Appl. Phys. Lett.* **2006**, *88* (2), 023113.
- (34) Lesik, M.; Spinicelli, P.; Pezzagna, S.; Happel, P.; Jacques, V.; Salord, O.; Rasser, B.; Delobbe, A.; Sudraud, P.; Tallaire, A.; Meijer, J.; Roch, J.-F. *Phys. Status Solidi A* **2013**, *210* (10), 2055–2059.
- (35) Weis, C. D.; Schuh, A.; Batra, A.; Persaud, A.; Rangelow, I. W.; Bokor, J.; Lo, C. C.; Cabrini, S.; Sideras-Haddad, E.; Fuchs, G. D.; Hanson, R.; Awschalom, D. D.; Schenkel, T. *Journal of Vacuum Science & Technology B: Microelectronics and Nanometer Structures* **2008**, *26* (6), 2596–2600.
- (36) Pezzagna, S.; Wildanger, D.; Mazarov, P.; Wieck, A. D.; Sarov, Y.; Rangelow, I.; Naydenov, B.; Jelezko, F.; Hell, S. W.; Meijer, J. *Small* **2010**, *6* (19), 2117–21.
- (37) Toyli, D. M.; Weis, C. D.; Fuchs, G. D.; Schenkel, T.; Awschalom, D. D. *Nano Lett.* **2010**, *10* (8), 3168–72.
- (38) Spinicelli, P.; Dréau, A.; Rondin, L.; Silva, F.; Achard, J.; Xavier, S.; Bansropun, S.; Debuisschert, T.; Pezzagna, S.; Meijer, J.; Jacques, V.; Roch, J. F. *New J. Phys.* **2011**, *13* (2), 025014.
- (39) Sangtawesin, S.; Brundage, T. O.; Atkins, Z. J.; Petta, J. R. *Appl. Phys. Lett.* **2014**, *105* (6), 063107.
- (40) Pezzagna, S.; Rogalla, D.; Becker, H. W.; Jakobi, I.; Dolde, F.; Naydenov, B.; Wrachtrup, J.; Jelezko, F.; Trautmann, C.; Meijer, J. *Phys. Status Solidi A* **2011**, *208* (9), 2017–2022.
- (41) Bayn, I.; Chen, E. H.; Trusheim, M. E.; Li, L.; Schroder, T.; Gaathon, O.; Lu, M.; Stein, A.; Liu, M.; Kisslinger, K.; Clevenson, H.; Englund, D. *Nano Lett.* **2015**, *15* (3), 1751–8.
- (42) Antonov, D.; Häußermann, T.; Aird, A.; Roth, J.; Trebin, H. R.; Müller, C.; McGuinness, L.; Jelezko, F.; Yamamoto, T.; Isoya, J.; Pezzagna, S.; Meijer, J.; Wrachtrup, J. *Appl. Phys. Lett.* **2014**, *104* (1), 012105.
- (43) Ziegler, J. F.; Ziegler, M. D.; Biersack, J. P. *Nucl. Instrum. Methods Phys. Res., Sect. B* **2010**, *268* (11–12), 1818–1823.
- (44) Mainwood, A. *Phys. Rev. B: Condens. Matter Mater. Phys.* **1994**, *49* (12), 7934–7940.
- (45) Santori, C.; Barclay, P. E.; Fu, K.-M. C.; Beausoleil, R. G. *Phys. Rev. B: Condens. Matter Mater. Phys.* **2009**, *79* (12), 125313.
- (46) Naydenov, B.; Reinhard, F.; Lämmlle, A.; Richter, V.; Kalish, R.; D’Haenens-Johansson, U. F. S.; Newton, M.; Jelezko, F.; Wrachtrup, J. *r. Appl. Phys. Lett.* **2010**, *97* (24), 242511.
- (47) Chu, Y.; de Leon, N. P.; Shields, B. J.; Hausmann, B.; Evans, R.; Togan, E.; Burek, M. J.; Markham, M.; Stacey, A.; Zibrov, A. S.; Yacoby, A.; Twitchen, D. J.; Loncar, M.; Park, H.; Maletinsky, P.; Lukin, M. D. *Nano Lett.* **2014**, *14* (4), 1982–6.
- (48) Ofori-Okai, B. K.; Pezzagna, S.; Chang, K.; Loretz, M.; Schirhagl, R.; Tao, Y.; Moores, B. A.; Groot-Berning, K.; Meijer, J.; Degen, C. L. *Phys. Rev. B: Condens. Matter Mater. Phys.* **2012**, *86* (8), 081406.
- (49) Chen, E. H.; Gaathon, O.; Trusheim, M. E.; Englund, D. *Nano Lett.* **2013**, *13* (5), 2073–7.
- (50) Rugar, D.; Mamin, H. J.; Sherwood, M. H.; Kim, M.; Rettner, C. T.; Ohno, K.; Awschalom, D. D. *Nat. Nanotechnol.* **2014**, *10* (2), 120–4.
- (51) DeVience, S. J.; Pham, L. M.; Lovchinsky, I.; Sushkov, A. O.; Bar-Gill, N.; Belthangady, C.; Casola, F.; Corbett, M.; Zhang, H.; Lukin, M.; Park, H.; Yacoby, A.; Walsworth, R. L. *Nat. Nanotechnol.* **2015**, *10* (2), 129–34.
- (52) Romach, Y.; Muller, C.; Unden, T.; Rogers, L. J.; Isoda, T.; Itoh, K. M.; Markham, M.; Stacey, A.; Meijer, J.; Pezzagna, S.; Naydenov, B.; McGuinness, L. P.; Bar-Gill, N.; Jelezko, F. *Phys. Rev. Lett.* **2015**, *114* (1), 017601.
- (53) Myers, B. A.; Das, A.; Dartiaill, M. C.; Ohno, K.; Awschalom, D. D.; Bleszynski Jayich, A. C. *Phys. Rev. Lett.* **2014**, *113* (2), 027602.
- (54) Staudacher, T.; Ziem, F.; Häußler, L.; Stöhr, R.; Steinert, S.; Reinhard, F.; Scharpf, J.; Denisenko, A.; Wrachtrup, J. *Appl. Phys. Lett.* **2012**, *101* (21), 212401.
- (55) Stacey, A.; O’Donnell, K. M.; Chou, J. P.; Schenk, A.; Tadich, A.; Dontschuk, N.; Cervenka, J.; Pakes, C.; Gali, A.; Hoffman, A.; Praver, S. *Adv. Mater. Interfaces* **2015**, *2* (10), 1500079.
- (56) Kim, M.; Mamin, H. J.; Sherwood, M. H.; Ohno, K.; Awschalom, D. D.; Rugar, D. *Phys. Rev. Lett.* **2015**, *115* (8), 087602.
- (57) Jamonneau, P.; Lesik, M.; Tétienne, J. P.; Alvizu, I.; Mayer, L.; Dreau, A.; Kosen, S.; Roch, J. F.; Pezzagna, S.; Meijer, J.; Teraji, T.; Kubo, Y.; Bertet, P.; Maze, J. R.; Jacques, V. *Phys. Rev. B: Condens. Matter Mater. Phys.* **2016**, *93* (2), 024305.
- (58) Schwartz, J.; Michaelides, P.; Weis, C. D.; Schenkel, T. *New J. Phys.* **2011**, *13* (3), 035022.
- (59) Wang, Z.-H.; Takahashi, S. *Phys. Rev. B: Condens. Matter Mater. Phys.* **2013**, *87* (11), 115122.

(60) Vieu, C.; Carcenac, F.; Pepin, A.; Chen, Y.; Mejias, M.; Lebib, A.; Manin-Ferlazzo, L.; Couraud, L.; Launois, H. *Appl. Surf. Sci.* **2000**, *164*, 111–117.

(61) Duan, H. G.; Winston, D.; Yang, J. K. W.; Cord, B. M.; Manfrinato, V. R.; Berggren, K. K. *J. Vac. Sci. Technol. B* **2010**, *28* (6), C6c58–C6c62.

(62) Park, J. H.; Ambwani, P.; Manno, M.; Lindquist, N. C.; Nagpal, P.; Oh, S. H.; Leighton, C.; Norris, D. J. *Adv. Mater.* **2012**, *24* (29), 3988–92.

(63) Waldherr, G.; Wang, Y.; Zaiser, S.; Jamali, M.; Schulte-Herbruggen, T.; Abe, H.; Ohshima, T.; Isoya, J.; Du, J. F.; Neumann, P.; Wrachtrup, J. *Nature* **2014**, *506* (7487), 204–7.